

An Investigation of the Intrinsic Force Sensing Capabilities of Continuum Robots

Kai Xu, *Student Member, IEEE*, and Nabil Simaan, *Member, IEEE*

Abstract—This paper presents the theoretical analysis and the experimental validation of the force sensing capabilities of continuum robots. These robots employ superelastic NiTi backbones and actuation redundancy. The paper uses screw theory to analyze the limitations and provide geometric interpretation to the sensible wrenches. The analysis is based on the singular value decomposition of the Jacobian mapping between the configuration space and the twist space of the end effector. The results show that the sensible wrenches belong to a 2-D screw system and the insensible wrenches belong to a 4-D screw system. The theory presented in this paper is validated through simulations and experiments. It is shown that the force sensing errors have an average of 0.34 g with a standard deviation of 0.83 g. Another experiment of generating the stiffness map of a silicone strip suggests possible medical application of palpation for tumor detection. The presented study allows force sensing in challenging environments where placing force sensors at the distal end of a robot is not possible due to limitations such as size and MRI compatibility.

Index Terms—Continuum robot, force sensing, screw theory, singular value decomposition (SVD), surgical assistance.

I. INTRODUCTION

DISTAL dexterity enhancement in minimally invasive surgery (MIS) is a key enabler for complex tasks in confined spaces [1]–[3]. Many works focused on various ways to overcome the dexterity constraints in MIS. These works included planar and spatial linkages [4]–[7], parallel wrists [8], [9], serial articulated wrists [10]–[12], and more recently, snake-like devices [4], [12]–[20] to allow surgeons to control the position and orientation of surgical tools. Distal dexterity enhancement was investigated in robotic systems for laparoscopy [11], [21], [22], arthroscopy [14], gastrointestinal surgery [13], [18], neurosurgery [16], fetal surgery [15], and ear, nose, and throat (ENT) surgery [23], etc. The different actuation methods for these devices included wire actuation [11], [15], [16], [19], shape memory alloy (SMA) actuation [14], mechanical actuation through linkages [5], [6], gear transmission [4], and our recent design that implements push–pull actuation using multiple superelastic tubes and beams [2], [24]–[26].

Manuscript received December 14, 2007; revised March 18, 2008. This paper was recommended for publication by Associate Editor B. J. Yi and Editor F. Park upon evaluation of the reviewers' comments. This work was supported in part by the National Science Foundation (NSF) under Engineering Research Center Grant EEC9731478 and NSF Grant IIS9801684, in part by the National Institutes of Health (NIH) under Grant R21 EB004457-01, and in part by the Columbia University.

The authors are with the Department of Mechanical Engineering, Columbia University, NY 10027 USA (e-mail: kx2102@columbia.edu; ns2236@columbia.edu).

Color versions of one or more of the figures in this paper are available online at <http://ieeexplore.ieee.org>.

Digital Object Identifier 10.1109/TRO.2008.924266

In contrast to these efforts for providing distal dexterity, most existing MIS robotic systems do not provide force feedback. Force feedback has been shown to be an important factor for improved patient safety, precise manipulation, grasping or palpation of soft organs, and for improved transparency in master/slave teleoperation for precise suture placement [27]–[32]. For this reason, many recent works focused on new surgical tools with force sensing capabilities [33]–[38]. These works focused on designing miniature force sensors to be placed at the distal end of the surgical devices or using joint-level information to quantify the applied forces. For example, Seibold *et al.* [36] developed a Ø10 mm miniature six-axis force sensor with force resolution of 0.25 N in z -direction and 0.05 N in x - and y -directions, which is mounted near the distal tip of the surgical tool. Tadano and Kawashima [37] presented a Ø10 mm forceps with force sensing ability by monitoring the pressure of a pneumatic actuator. An accuracy of 0.05 N was obtained.

Placing a dedicated multiaxis force sensor at the tip of surgical end effectors offers a direct measurement of the interaction forces. However, the increased demands for MRI compatibility and for smaller surgical end effectors limit this approach. This paper answers this need for developing down-scalable surgical devices that can provide force feedback without using force sensors located proximal to the end effectors. This type of force sensing using joint-level information is hereby referred to as “*intrinsic force sensing*.”

Fig. 1 shows a continuum robot and its actuation unit. This experimental setup was constructed to validate the possible use of joint-level force information to sense the wrench applied at the distal end of the robot. The diameter of this robot is 7.5 mm. It has four superelastic NiTi tubes as its backbones (shown clearly in Fig. 2). One primary backbone (see Fig. 1⑤) is centrally located and is attached to the base disk (see Fig. 1③) and the end disk (see Fig. 1①). Three identical secondary backbones (see Fig. 1④) are equidistant from each other and from the primary backbone. The secondary backbones are only attached to the end disk and can slide in appropriately toleranced holes in the base disk and in the spacer disks (see Fig. 1②). In order to minimize the frictions in the system, the spacer disks are made from polytetrafluoroethylene (PTFE) while PTFE bushing is also implemented in the base disk. Each secondary backbone is actuated in push–pull mode by an actuation rod (see Fig. 1⑥). The actuation force is continuously monitored by low-cost load cells Omega-LC703 (see Fig. 1⑧). An actuation cantilever (Fig. 1⑦) drives the load cell and the actuation rod. The actuation cantilever equips linear ball bearings and can slide freely along the actuation rails. A double-supported actuation slider (see Fig. 1⑨) is connected to the load cells to drive the actuation cantilevers. All the actuation components and load cells

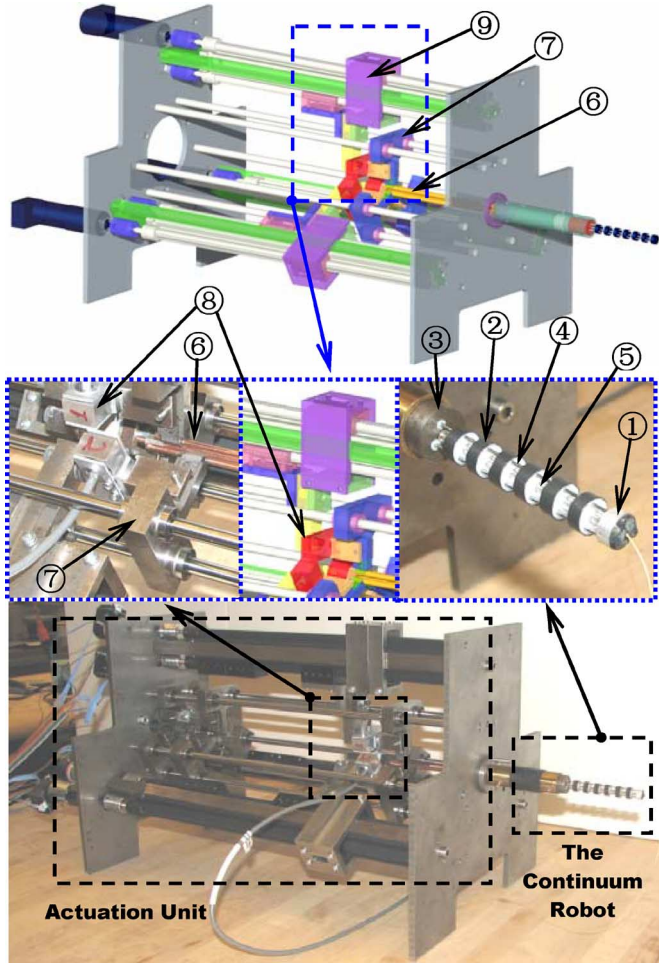


Fig. 1. Ø7.5 mm continuum robot. ① End disk. ② Spacer disk. ③ Base disk. ④ Secondary backbone. ⑤ Primary backbone. ⑥ Actuation rods. ⑦ Actuation cantilever with linear ball bearings. ⑧ Load cells. ⑨ Double-supported actuation sliders.

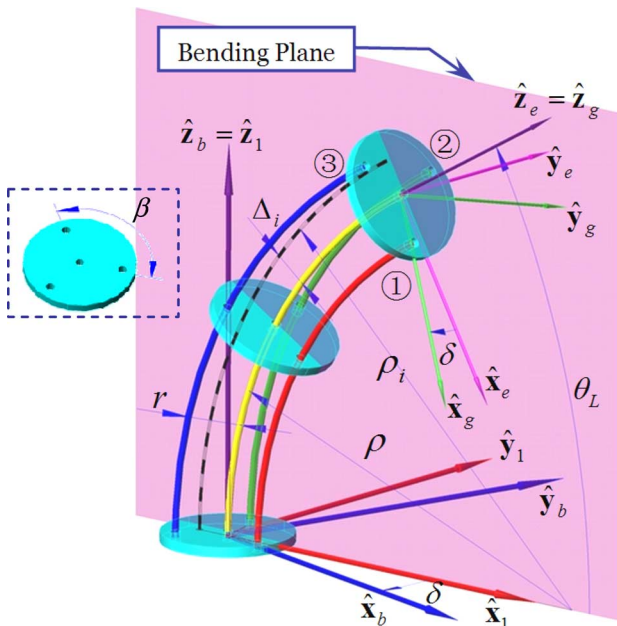


Fig. 2. Kinematics nomenclature with the definition of the configuration variable δ for a bent robot.

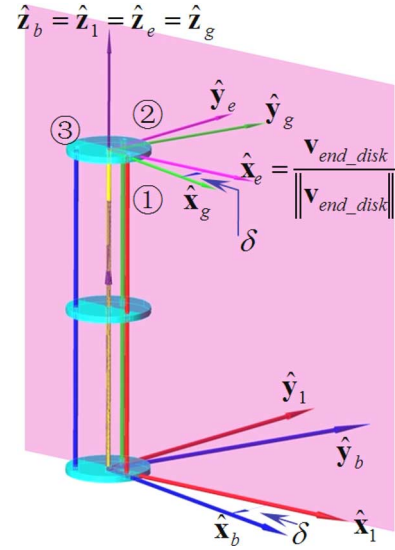


Fig. 3. Kinematics nomenclature with the definition of the configuration variable δ for a straight robot.

were designed to be rigid enough so that their deformations can be neglected. Two degrees of freedom bending motion of the continuum robot is achieved through simultaneous actuation of the three secondary backbones.

This design is inspired by the works of Hirose [39], and Walker and Gravagne [40], [41] in which a single flexible backbone was actuated by wires. Our previous work [25] showed that using multiple backbones in push–pull actuation offers some advantages over the wire-actuated snake-like robots. These advantages include backlash elimination, enhanced down-scalability, and improved payload. Although this design presents difficulties in modeling and control due to the flexibility of the actuation elements, it also offers the possibility to sense exerted external wrenches by monitoring the actuation forces on the secondary backbones.

A. Contribution

The main contribution of this paper is given in Section II where the force sensing capabilities of the continuum robot are analyzed. A geometric interpretation using screw theory and singular value decomposition (SVD) of a kinematic mapping between a 2-D configuration space and the 6-D twist space of the end effector is presented. It is shown that the sensible wrenches belong to a 2-D screw system. Other contributions include using experimental results to correct the kinematics, statics, and force sensing models, presented in Section III. In Section IV, the corrected force sensing models are validated through experiments.

II. MODELING OF THE CONTINUUM ROBOT

A. Nomenclature

The continuum robot is shown in Figs. 2 and 3. Table I presents the nomenclature used in this paper. Four coordinate systems are defined to describe the kinematics of the robot.

- 1) *Base disk coordinate system (BDS)*: $\{\hat{x}_b, \hat{y}_b, \hat{z}_b\}$ is attached to the base disk, whose XY -plane is defined to

TABLE I
NOMENCLATURE USED IN THIS PAPER

i	Index of the secondary backbones, $i = 1, 2, 3$
s	Arc-length parameter of the primary backbone
L, L_i	Length of the primary and the i^{th} secondary backbone measured from the base disk to the end disk
q_i	Joint parameter of the i^{th} secondary backbone $q_i = L_i - L$
r	Radius of the pitch circle defining the positions of the secondary backbones in all the disks.
β	Division angle of the secondary backbones along the circumference of the pitch circle, $\beta = 2\pi/3$
$\rho(s)$	Radius of curvature of the primary backbone
$\rho_i(s)$	Radius of curvature of the i^{th} secondary backbone
$\theta(s)$	The angle of the tangent to the primary backbone in the bending plane. $\theta _{s=L}$ and $\theta _{s=0}$ are designated by θ_L and θ_0 , respectively. NOTE: $\theta_0 = \pi/2$ is a constant.
δ_i	A right-handed rotation angle from $\hat{\mathbf{x}}_1$ about $\hat{\mathbf{z}}_1$ to a line passing through the primary backbone and the i^{th} secondary backbone at $s = 0$. At a straight configuration $\hat{\mathbf{x}}_1$ is along the same direction as the desired instantaneous linear velocity of the end disk.
δ	$\delta \equiv \delta_1$ and $\delta_i = \delta + (i-1)\beta$, $i = 1, 2, 3$
Δ_i	Radial offset from primary backbone to the projection of the i^{th} secondary backbone on the bending plane.
\mathbf{J}_{yx}	Jacobian matrix of the mapping $\dot{\mathbf{y}} = \mathbf{J}_{yx}\dot{\mathbf{x}}$ where the dot over the variable represents time derivative.
E_p, E_s	Young's modulus of the primary and the secondary backbones.
I_p, I_s	Cross-sectional moments of inertia of the primary and the secondary backbones
$\boldsymbol{\tau}$	Actuation forces of the secondary backbones $\boldsymbol{\tau} \in \mathfrak{R}^{3 \times 1}$.
${}^1\mathbf{R}_2$	Rotation matrix of frame 2 with respect to frame 1.
${}^b\mathbf{p}$	Position vector of the robot tip in the BDS
$\dot{\mathbf{x}}$	The twist $\dot{\mathbf{x}} \in \mathfrak{R}^{6 \times 1}$ of the end disk in a frame instantaneously parallel to BDS and centered at center of the end disk. $\dot{\mathbf{x}}$ is defined with the linear velocity vector preceding the angular velocity vector.

coincide with the upper surface of the base disk and its origin is at the center of the base disk. The $\hat{\mathbf{x}}_b$ points from the center of the base disk to the first secondary backbone while the $\hat{\mathbf{z}}_b$ is perpendicular to the base disk. The three secondary backbones are numbered according to the definition of δ_i .

- 2) *Bending plane coordinate system (BPS)*: $\{\hat{\mathbf{x}}_1, \hat{\mathbf{y}}_1, \hat{\mathbf{z}}_1\}$ is defined such that the continuum robot bends in the XZ-plane, with its origin coinciding with the origin of BDS.
- 3) *End disk coordinate system (EDS)*: $\{\hat{\mathbf{x}}_e, \hat{\mathbf{y}}_e, \hat{\mathbf{z}}_e\}$ is obtained from BPS by a rotation about $\hat{\mathbf{y}}_1$ such that $\hat{\mathbf{z}}_1$ becomes the backbone tangent at the end disk. The origin of EDS is at the center of the end disk.
- 4) *Gripper coordinate system (GCS)*: $\{\hat{\mathbf{x}}_g, \hat{\mathbf{y}}_g, \hat{\mathbf{z}}_g\}$ is attached to an imaginary gripper affixed to the end disk. $\hat{\mathbf{x}}_g$ points from the center of the end disk to the first secondary backbone and $\hat{\mathbf{z}}_g$ is normal to the end disk. GCS is obtained by a right-handed rotation about $\hat{\mathbf{z}}_e$.

B. Kinematics Model

The generalized solution for the inverse kinematics of hyper redundant robots was given in [42]–[45]. The kinematics of continuum robots was addressed in [2], [41], [46], and [47], in which the bending shape of the continuum robot was assumed to be circular. For completeness, the explicit closed form of the kinematics is summarized here, based on [2].

The configuration of the continuum robot is parameterized by θ_L and δ angles. The inverse kinematics is provided in [2] and [25] and in Appendix A

$$L_i = L + q_i = L + \Delta_i(\theta_L - \theta_0) \quad (1)$$

$$\Delta_i \equiv r \cos(\delta_i), \quad i = 1, 2, \text{ and } 3. \quad (2)$$

For a given q_i , the robot configuration $\boldsymbol{\psi} = [\theta_L \quad \delta]^T$ is given by [25]. The function atan2 in (4) follows the convention in [48]

$$\theta_L = \theta_0 + \frac{q_i}{\Delta_i} \quad (3)$$

$$\delta = \text{atan2}(q_2 - q_1 \cos\beta, -q_1 \sin\beta). \quad (4)$$

The instantaneous direct kinematics is then given by

$$\dot{\mathbf{x}} = \mathbf{J}_{x\psi}\dot{\boldsymbol{\psi}}. \quad (5)$$

Since the robot includes flexible members, its shape is determined by the minimal energy solution. In this paper, we assume a circular arc shape. This assumption is experimentally validated in Section III. The Jacobian matrix is shown below, with derivation details in Appendix B:

$$\mathbf{J}_{x\psi} = \begin{bmatrix} Lc_\delta \frac{(\theta_L - \theta_0)c_{\theta_L} - s_{\theta_L} + 1}{(\theta_L - \theta_0)^2} & -L \frac{s_\delta (s_{\theta_L} - 1)}{\theta_L - \theta_0} \\ -Ls_\delta \frac{(\theta_L - \theta_0)c_{\theta_L} - s_{\theta_L} + 1}{(\theta_L - \theta_0)^2} & -L \frac{c_\delta (s_{\theta_L} - 1)}{\theta_L - \theta_0} \\ L \frac{(\theta_L - \theta_0)s_{\theta_L} + c_{\theta_L}}{(\theta_L - \theta_0)^2} & 0 \\ -s_\delta & c_\delta c_{\theta_L} \\ -c_\delta & -s_\delta c_{\theta_L} \\ 0 & -1 + s_{\theta_L} \end{bmatrix}. \quad (6)$$

Equation (6) is ill-defined when $\theta_L = \theta_0 = \pi/2$. This singularity for the configurations $\theta_L = \theta_0 = \pi/2$ is resolved by applying L'Hopital Rule, as in (7). For these configurations, the robot bending plane is defined according to the desired linear velocity of the end disk, as shown in Fig. 3:

$$\lim_{\theta_L \rightarrow \theta_0 = \pi/2} \mathbf{J}_{x\psi} = \begin{bmatrix} -(L/2)c_\delta & 0 \\ (L/2)s_\delta & 0 \\ 0 & 0 \\ -s_\delta & 0 \\ -c_\delta & 0 \\ 0 & 0 \end{bmatrix}. \quad (7)$$

The instantaneous inverse kinematics is given as

$$\dot{\boldsymbol{\psi}} = \mathbf{J}_{q\psi}\dot{\mathbf{q}}. \quad (8)$$

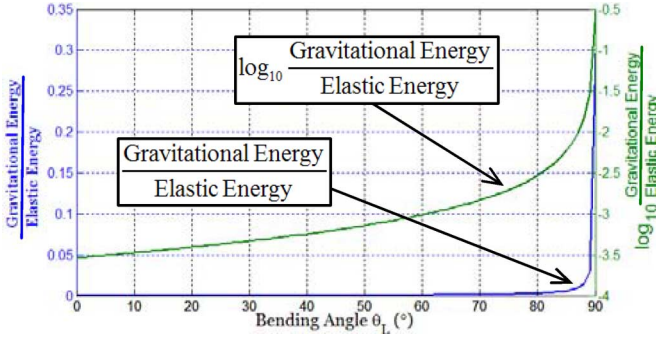


Fig. 4. Gravitational energy over elastic energy ratio.

By taking the derivative of (1) for q_i , $i = 1, 2$, and 3

$$\mathbf{J}_{\mathbf{q}\psi} = \begin{bmatrix} r \cos(\delta) & -r(\theta_L - \theta_0) \sin(\delta) \\ r \cos(\delta + \beta) & -r(\theta_L - \theta_0) \sin(\delta + \beta) \\ r \cos(\delta + 2\beta) & -r(\theta_L - \theta_0) \sin(\delta + 2\beta) \end{bmatrix}. \quad (9)$$

C. Virtual Work Model

The static analysis is based on a virtual work model. Twisting, extension of backbones, and friction are neglected. Each PTFE spacer disk of the robot in Fig. 1 weighs 0.23 g and the aluminum end disk weighs 0.39 g. Density of NiTi is 6.2 g/cm³. Given the circular bending shape of the continuum robot, the ratio of gravitational energy to elastic energy as a function of the angle θ_L is plotted in Fig. 4. The gravitational energy is calculated when the robot is placed horizontally as in Fig. 1. This arrangement introduces the biggest gravitational energy change. Even thus, when the robot is only bent to $\theta_L = 87^\circ$, the ratio is as small as 0.0099 (0.99%). Hence, gravity is also neglected in the analysis.

Given the aforementioned assumptions, according to [49], the elastic energy of the continuum robot is given by

$$E = \int_L \frac{EI}{2} \left(\frac{d\theta}{ds} \right)^2 ds = (\theta_L - \theta_0)^2 \left(\frac{E_p I_p}{2L} + \sum_{i=1}^3 \left(\frac{E_s I_s}{2L_i} \right) \right). \quad (10)$$

Assume that an external wrench $\mathbf{W}_e = [\mathbf{f}_e^T \quad \mathbf{m}_e^T]^T$ acts on the end disk where \mathbf{f}_e indicates the force and \mathbf{m}_e the moment. This external wrench perturbs the robot posture (position and orientation) of the end disk by $\Delta \mathbf{x}$. To this pose perturbation, there is a corresponding change in the lengths of the secondary backbones $\Delta \mathbf{q} = [\Delta q_1 \quad \Delta q_2 \quad \Delta q_3]^T$. The actuation forces on the secondary backbones that maintain the equilibrium are $\boldsymbol{\tau} = [\tau_1 \quad \tau_2 \quad \tau_3]^T$. The change in the potential energy ΔE that corresponds to $\Delta \mathbf{x}$ is given by

$$\mathbf{W}_e^T \Delta \mathbf{x} + \boldsymbol{\tau}^T \Delta \mathbf{q} = \Delta E. \quad (11)$$

The virtual displacement is characterized by $\Delta \boldsymbol{\psi} = [\Delta \theta_L \quad \Delta \delta]^T$.

Using (5) and (8), the virtual work principle is rewritten as in (12). The equilibrium condition requires the terms associated with each independent DOF to vanish. The matrix form

of this system of linear equations is given in (13) where ∇E represents the gradient of the elastic energy with respect to the configuration perturbation $\Delta \boldsymbol{\psi}$

$$\mathbf{W}_e^T \mathbf{J}_{\mathbf{x}\psi} \Delta \boldsymbol{\psi} + \boldsymbol{\tau}^T \mathbf{J}_{\mathbf{q}\psi} \Delta \boldsymbol{\psi} - \nabla E^T \Delta \boldsymbol{\psi} = \mathbf{0} \quad (12)$$

$$\mathbf{J}_{\mathbf{q}\psi}^T \boldsymbol{\tau} + \mathbf{J}_{\mathbf{x}\psi}^T \mathbf{W}_e = \nabla E. \quad (13)$$

For the actuation forces, a redundancy resolution of (13) is obtained in [25] as

$$\boldsymbol{\tau} = (\mathbf{J}_{\mathbf{q}\psi}^T)^+ (\nabla E - \mathbf{J}_{\mathbf{x}\psi}^T \mathbf{W}_e) + \left(\mathbf{I} - (\mathbf{J}_{\mathbf{q}\psi}^T)^+ \mathbf{J}_{\mathbf{q}\psi}^T \right) \boldsymbol{\xi} \quad (14)$$

where $\boldsymbol{\xi} \in \mathbb{R}^{3 \times 1}$ is a vector of homogeneous actuation forces used to optimize the loads on the backbones and

∇E

$$= \begin{bmatrix} (\theta_L - \theta_0) \left(\frac{E_p I_p}{L} + \sum_{i=1}^3 \frac{E_s I_s}{L_i} \right) - \frac{(\theta_L - \theta_0)^2}{2} E_s I_s r \sum_{i=1}^3 \frac{\cos \delta_i}{L_i^2} \\ \frac{(\theta_L - \theta_0)^3}{2} E_s I_s r \sum_{i=1}^3 \frac{\sin \delta_i}{L_i^2} \end{bmatrix}.$$

In the compensated actuation of the continuum robot, one redundancy resolution is adopted as in [26]

$$\boldsymbol{\tau} = \mathbf{J}_{\mathbf{q}\psi} (\mathbf{J}_{\mathbf{q}\psi}^T \mathbf{J}_{\mathbf{q}\psi})^{-1} (\nabla E - \mathbf{J}_{\mathbf{x}\psi}^T \mathbf{W}_e). \quad (15)$$

D. Force Sensing Model

Equation (13) can be rewritten as

$$\mathbf{J}_{\mathbf{x}\psi}^T \mathbf{W}_e = \nabla E - \mathbf{J}_{\mathbf{q}\psi}^T \boldsymbol{\tau}. \quad (16)$$

It is possible for the continuum robot to have force sensing capability if the actuation forces $\boldsymbol{\tau}$ are measured by the load cells in Fig. 1. There are six unknown wrench components in \mathbf{W}_e while there are only two independent equations in (16). A solution of this underconstrained system of equations is obtained as in (17), where \mathbf{W}_s is the sensed external wrench, $\mathbf{N} = (\mathbf{I} - (\mathbf{J}_{\mathbf{x}\psi}^T)^+ (\mathbf{J}_{\mathbf{x}\psi}^T))$ is the null-space projector of $\mathbf{J}_{\mathbf{x}\psi}^T$, and $(\mathbf{J}_{\mathbf{x}\psi}^T)^+ = \mathbf{J}_{\mathbf{x}\psi} (\mathbf{J}_{\mathbf{x}\psi}^T \mathbf{J}_{\mathbf{x}\psi})^{-1}$. For any $\boldsymbol{\eta} \in \mathbb{R}^{6 \times 1}$, $\mathbf{J}_{\mathbf{x}\psi}^T \mathbf{N} \boldsymbol{\eta}$ does not affect the static equilibrium of the continuum robot. Accordingly, we split \mathbf{W}_s into a component \mathbf{W}_{sb} designating sensible wrenches and a component \mathbf{W}_{isb} representing wrenches that do not affect the joint-level forces $\boldsymbol{\tau}$, and hence, cannot be sensed (see (18))

$$\mathbf{W}_s = (\mathbf{J}_{\mathbf{x}\psi}^T)^+ (\nabla E - \mathbf{J}_{\mathbf{q}\psi}^T \boldsymbol{\tau}) + \mathbf{N} \boldsymbol{\eta} \quad (17)$$

$$\mathbf{W}_s = \mathbf{W}_{\text{sb}} + \mathbf{W}_{\text{isb}} \quad (18)$$

where $\mathbf{W}_{\text{sb}} = (\mathbf{J}_{\mathbf{x}\psi}^T)^+ (\nabla E - \mathbf{J}_{\mathbf{q}\psi}^T \boldsymbol{\tau})$ and $\mathbf{W}_{\text{isb}} = \mathbf{N} \boldsymbol{\eta}$.

The resolution for \mathbf{W}_s in (17) depends on the joint-level information and on an *a priori* knowledge. The *a priori* knowledge leads to the homogenous solution $\mathbf{N} \boldsymbol{\eta}$ while the joint-level information leads to $(\mathbf{J}_{\mathbf{x}\psi}^T)^+ (\nabla E - \mathbf{J}_{\mathbf{q}\psi}^T \boldsymbol{\tau})$. Although there may be several other sources of extrinsic information or *a priori* knowledge, in this paper we only consider *a priori* knowledge

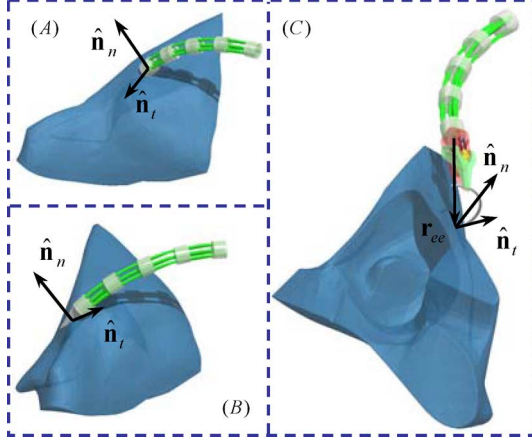


Fig. 5. Incorporation of the force sensing in a clinical environment. (A) Palpation. (B) Incision. (C) Suture penetration.

that stems from the geometry of the contact between the robot and its environment. As described in [50] different types of contacts (e.g., point, line, plane contacts with or without friction) are associated with different wrenches. Each type of contact geometry provides information about certain null components of the wrench that acts on the robot. $\mathbf{W}_{se} \in \mathbb{R}^{6 \times 1}$ is used to designate the *a priori* wrench estimate with these null components, while $\mathbf{S}_e \in \mathbb{R}^{6 \times 6}$ is used to designate the weights. Determining \mathbf{W}_s can be modeled as a constrained least squares problem, as shown in (19):

$$\begin{aligned} \eta &= \operatorname{argmin}((\mathbf{W}_s - \mathbf{W}_{se})^T \mathbf{S}_e (\mathbf{W}_s - \mathbf{W}_{se})) \\ \text{s.t. } \mathbf{W}_s &= (\mathbf{J}_{x\psi}^T)^+ (\nabla \mathbf{E} - \mathbf{J}_{q\psi}^T \boldsymbol{\tau}) + (\mathbf{I} - (\mathbf{J}_{x\psi}^T)^+ (\mathbf{J}_{x\psi}^T)) \eta. \end{aligned} \quad (19)$$

Equation (19) has a closed-form solution

$$\eta = \mathbf{N}^+ \mathbf{N}^T \mathbf{S}_e (\mathbf{W}_{se} - (\mathbf{J}_{x\psi}^T)^+ (\nabla \mathbf{E} - \mathbf{J}_{q\psi}^T \boldsymbol{\tau})) \quad (20)$$

where $\mathbf{N} = (\mathbf{I} - (\mathbf{J}_{x\psi}^T)^+ (\mathbf{J}_{x\psi}^T))$ and $\mathbf{N}^+ = (\mathbf{J}_{x\psi}^T)^+ \mathbf{S}_e (\mathbf{I} - (\mathbf{J}_{x\psi}^T)^+ (\mathbf{J}_{x\psi}^T))$.

In the case of palpation shown in Fig. 5(A), the possible contact geometries to be considered are soft finger contact or point contact with friction. For simplicity, point contact with friction is assumed. In this case, the moment components of the external wrench \mathbf{W}_e are all zero. The reaction force lies in a plane that is determined by the tissue surface normal $\hat{\mathbf{n}}_n$ and the local surface tangent $\hat{\mathbf{n}}_t$ that is opposite to the direction of the slippage between the robot and the tissue. $\hat{\mathbf{n}}_n$ and $\hat{\mathbf{n}}_t$ can be obtained by integrated vision. \mathbf{W}_{se} and \mathbf{S}_e can then be formulated as in (21), where c_t and c_n are any arbitrary real numbers. After substituting (21) into (19), the specific optimization problem as described in (22) is obtained. In (22), \mathbf{f}_s and \mathbf{m}_s are force and moment components of the sensed wrench \mathbf{W}_s . Clearly, the minimization leads to $\mathbf{f}_s^T (\hat{\mathbf{n}}_t \times \hat{\mathbf{n}}_n) (\hat{\mathbf{n}}_t \times \hat{\mathbf{n}}_n)^T \mathbf{f}_s = 0$ and $\mathbf{m}_s^T \mathbf{m}_s = 0$, as consistent with a \mathbf{W}_s that stems from a point contact, i.e., all moment components are zero and the force lies

in the plane defined by $\hat{\mathbf{n}}_n$ and $\hat{\mathbf{n}}_t$:

$$\begin{aligned} \mathbf{S}_e &= \begin{bmatrix} (\hat{\mathbf{n}}_t \times \hat{\mathbf{n}}_n) (\hat{\mathbf{n}}_t \times \hat{\mathbf{n}}_n)^T & \mathbf{0}_{1 \times 3} \\ \mathbf{0}_{3 \times 3} & \mathbf{I}_{3 \times 3} \end{bmatrix} \quad \text{and} \\ \mathbf{W}_{se} &= \begin{bmatrix} c_t \hat{\mathbf{n}}_t + c_n \hat{\mathbf{n}}_n \\ \mathbf{0}_{3 \times 1} \end{bmatrix} \\ \eta &= \operatorname{argmin}(\mathbf{f}_s^T (\hat{\mathbf{n}}_t \times \hat{\mathbf{n}}_n) (\hat{\mathbf{n}}_t \times \hat{\mathbf{n}}_n)^T \mathbf{f}_s + \mathbf{m}_s^T \mathbf{m}_s) \\ \text{s.t. } \mathbf{W}_s &= (\mathbf{J}_{x\psi}^T)^+ (\nabla \mathbf{E} - \mathbf{J}_{q\psi}^T \boldsymbol{\tau}) + (\mathbf{I} - (\mathbf{J}_{x\psi}^T)^+ (\mathbf{J}_{x\psi}^T)) \eta. \end{aligned} \quad (21)$$

For example, if the plane defined by $\hat{\mathbf{n}}_n$ and $\hat{\mathbf{n}}_t$ is parallel to the XY -plane of BDS, then $\mathbf{S}_e = \operatorname{diag}(0, 0, 1, 1, 1, 1)$ and $\mathbf{W}_{se} = [c_t \ c_n \ 0 \ 0 \ 0 \ 0]^T$. This case corresponds to the two experiments presented in Section IV.

In the case of incision shown in Fig. 5(B) or the case of suture penetration shown in Fig. 5(C), a line contact or a plane contact should be assumed. Additional interaction wrench information needs to be added into the formulation of \mathbf{S}_e and \mathbf{W}_{se} . The new formulation will depend on the geometry of the end effector, the information from other wrench sensors or the model of the tissue, and a measurement of the tissue deflection from vision.

We next seek to understand the physical interpretations for \mathbf{W}_{sb} and \mathbf{W}_{isb} . The SVD of $\mathbf{J}_{x\psi}$ from (23) is used for this purpose. In (23), the matrix $\mathbf{D}_x = [\operatorname{diag}(d_1, d_2) \ \mathbf{0}_{2 \times 4}]^T$ is the matrix of singular values, $\mathbf{U}_x \in \mathbb{R}^{6 \times 6}$ and $\mathbf{V}_x \in \mathbb{R}^{2 \times 2}$ are unitary orthogonal matrices designating the left (output) singular vectors and right (input) singular vectors of $\mathbf{J}_{x\psi} \in \mathbb{R}^{6 \times 2}$, respectively. Available in [51], the pseudoinverse of $\mathbf{J}_{x\psi}$ is expressed using the SVD as in (24). After substituting (15) into (18) and simplifying terms, we obtain the result in (25). The disappearance of $\mathbf{J}_{q\psi}$ and $\nabla \mathbf{E}$ in (25) is due to using the specific actuation redundancy resolution of (15). After substituting the SVD of $\mathbf{J}_{x\psi}$ into (25), we obtain (26) that expresses \mathbf{W}_{sb} and \mathbf{W}_{isb} in terms of the left singular vectors of $\mathbf{J}_{x\psi}$. By using the property of orthogonal matrix, $\mathbf{I} = \mathbf{U}_x \mathbf{U}_x^T$, (26) can be simplified as in (27) and (28) where \mathbf{u}_x^i designates the i th column of \mathbf{U}_x . In (27), we note that \mathbf{N} is the null space projector of $\mathbf{J}_{x\psi}^T$, $\mathbf{N} = (\mathbf{I} - (\mathbf{J}_{x\psi}^T)^+ (\mathbf{J}_{x\psi}^T)) = \mathbf{U}_x \hat{\mathbf{I}} \mathbf{U}_x^T$.

$$\mathbf{J}_{x\psi} = \mathbf{U}_x \mathbf{D}_x \mathbf{V}_x^T \quad (23)$$

$$(\mathbf{J}_{x\psi}^T)^+ = \mathbf{U}_x \tilde{\mathbf{D}}_x \mathbf{V}_x^T \quad (24)$$

where $\tilde{\mathbf{D}}_x = [\operatorname{diag}(1/d_1, 1/d_2) \ \mathbf{0}_{2 \times 4}]^T$

$$\mathbf{W}_{sb} = (\mathbf{J}_{x\psi}^T)^+ \mathbf{J}_{x\psi}^T \mathbf{W}_e, \quad \mathbf{W}_{isb} = \mathbf{N} \boldsymbol{\eta} \quad (25)$$

$$\mathbf{W}_{sb} = \mathbf{U}_x \tilde{\mathbf{I}} \mathbf{U}_x^T \mathbf{W}_e, \quad \mathbf{W}_{isb} = (\mathbf{I} - \mathbf{U}_x \tilde{\mathbf{I}} \mathbf{U}_x^T) \boldsymbol{\eta} \quad (26)$$

where $\tilde{\mathbf{I}} \equiv \operatorname{diag}(1, 1, 0, 0, 0, 0)$ and $\hat{\mathbf{I}} \equiv \mathbf{I} - \tilde{\mathbf{I}} = \operatorname{diag}(0, 0, 1, 1, 1, 1)$

$$\mathbf{W}_{sb} = \mathbf{U}_x \tilde{\mathbf{I}} \mathbf{U}_x^T \mathbf{W}_e, \quad \mathbf{W}_{isb} = \mathbf{U}_x \hat{\mathbf{I}} \mathbf{U}_x^T \boldsymbol{\eta} \quad (27)$$

$$\mathbf{W}_{sb} = \mathbf{U}_x \tilde{\mathbf{U}}_x \mathbf{W}_e, \quad \mathbf{W}_{isb} = \mathbf{U}_x \hat{\mathbf{U}}_x^T \boldsymbol{\eta} \quad (28)$$

where

$$\tilde{\mathbf{U}}_{\mathbf{x}} \equiv \tilde{\mathbf{I}}\mathbf{U}_{\mathbf{x}}^T = \begin{bmatrix} (\mathbf{u}_{\mathbf{x}}^1)^T \\ (\mathbf{u}_{\mathbf{x}}^2)^T \\ \mathbf{0} \\ \mathbf{0} \\ \mathbf{0} \\ \mathbf{0} \end{bmatrix}$$

and

$$\hat{\mathbf{U}}_{\mathbf{x}} \equiv \hat{\mathbf{I}}\mathbf{U}_{\mathbf{x}}^T = \begin{bmatrix} \mathbf{0} \\ \mathbf{0} \\ (\mathbf{u}_{\mathbf{x}}^3)^T \\ (\mathbf{u}_{\mathbf{x}}^4)^T \\ (\mathbf{u}_{\mathbf{x}}^5)^T \\ (\mathbf{u}_{\mathbf{x}}^6)^T \end{bmatrix}.$$

In (28), the first term $\mathbf{U}_{\mathbf{x}}\tilde{\mathbf{U}}_{\mathbf{x}}\mathbf{W}_e$ depends on the geometry of the robot (through $\mathbf{U}_{\mathbf{x}}$) and on the applied wrench \mathbf{W}_e . The second term $\mathbf{U}_{\mathbf{x}}\hat{\mathbf{U}}_{\mathbf{x}}\boldsymbol{\eta}$ does not affect the joint-level sensor information $\boldsymbol{\tau}$; thus, our focus will mainly be on the first term $\mathbf{U}_{\mathbf{x}}\tilde{\mathbf{U}}_{\mathbf{x}}\mathbf{W}_e$.

Since $\mathbf{u}_{\mathbf{x}}^i$ ($i = 1, \dots, 6$) are the left singular vectors of $\mathbf{J}_{\mathbf{x}\psi}$, they represent twists in axial Plücker coordinates, which is consistent with the definition of $\dot{\mathbf{x}}$. The reciprocal product [52] of screws $\$1$ and $\$2$ is given by $\$1^T \2 , where for a general screw, $\$ = [s_1 \ s_2 \ s_3 \ s_4 \ s_5 \ s_6]^T$ and its transpose $\$^T = [s_4 \ s_5 \ s_6 \ s_1 \ s_2 \ s_3]$. Using this definition, the components of $\tilde{\mathbf{U}}_{\mathbf{x}}\mathbf{W}_e$ are interpreted as reciprocal products $(\mathbf{u}_{\mathbf{x}}^i)^T \mathbf{W}_e$ ($i = 1$ and 2). If a wrench \mathbf{W}_e is reciprocal to $\mathbf{u}_{\mathbf{x}}^i$ for $i = 1$ and 2 , it cannot be sensed; otherwise, \mathbf{W}_e will affect the joint-level forces $\boldsymbol{\tau}$ and it will be sensible. Based on this interpretation, the decomposition of \mathbf{W}_s into \mathbf{W}_{sb} and \mathbf{W}_{isb} can be characterized as

$$\mathbf{W}_{\text{sb}}^T \mathbf{u}_{\mathbf{x}}^i \neq \mathbf{0} \quad \text{and} \quad \mathbf{W}_{\text{isb}}^T \mathbf{u}_{\mathbf{x}}^i = \mathbf{0}, \quad \text{for } i = 1 \text{ and } 2. \quad (29)$$

From (29), it is evident that the insensible wrenches \mathbf{W}_{isb} belong to a 4-D wrench system $\{\mathbf{W}_{\text{isb}}\}$ reciprocal to $\mathbf{u}_{\mathbf{x}}^i$ ($i = 1, 2$). The sensible wrenches \mathbf{W}_{sb} belong to a 2-D wrench system that is reciprocal to $\mathbf{u}_{\mathbf{x}}^i$ ($i = 3, \dots, 6$). Also from (25) and (28), one concludes

$$\{\mathbf{W}_{\text{isb}}\} = \text{Nul}(\mathbf{J}_{\mathbf{x}\psi}^T) \quad (30)$$

where $\text{Nul}(\mathbf{A})$ is the null space of \mathbf{A} .

The matrix $\mathbf{u}_{\mathbf{x}}^i$ can be rewritten in Plücker ray coordinates as in (31) where $[\hat{\mathbf{n}}^T, (\mathbf{r}_o \times \hat{\mathbf{n}})^T]^T$ is the Plücker coordinates of the screw axis and λ is its pitch [53]. $\mathbf{u}_{\mathbf{x}}^i$ can then be visualized as a line segment of $[\hat{\mathbf{n}}^T, (\mathbf{r}_o \times \hat{\mathbf{n}})^T]^T$ with its length equal to λ , starting from a point \mathbf{r}_o that expressed in a coordinate system parallel to BDS and centered at the center of the end disk. The linear combinations of $\mathbf{u}_{\mathbf{x}}^i$ ($i = 1, 2$) can be visualized as a rank 2 screw system (cylindroid) [53], [54]. This cylindroid represents the sensible wrenches \mathbf{W}_{sb} . At the same time, the

TABLE II
PARAMETERS OF THE ROBOT IN FIG. 1

$L = 50\text{mm}$	$r = 3.0\text{mm}$	$E_p = E_s = E = 62\text{GPa}$
$d_{op} = d_{os} = 0.889\text{mm}$		$d_{ip} = d_{is} = 0.762\text{mm}$

basis wrenches that span the insensible wrench space $\{\mathbf{W}_{\text{isb}}\}$ can also be visualized

$$\mathbf{u}_{\mathbf{x}}^i = \kappa_s \begin{bmatrix} \hat{\mathbf{n}} \\ \mathbf{r}_o \times \hat{\mathbf{n}} + \lambda \hat{\mathbf{n}} \end{bmatrix}. \quad (31)$$

The essence of the proposed force sensing analysis can now be pictured: for any external wrench \mathbf{W}_e , its projection in the sensible wrench space $\{\mathbf{W}_{\text{sb}}\}$ is calculated from (17) as $\boldsymbol{\eta} = \mathbf{0}$; its projection in the insensible wrench space $\{\mathbf{W}_{\text{isb}}\}$ is calculated from (19) making use of the other sensory information or *a priori* knowledge.

E. Simulation Case Studies

This section presents a simulation and visualization of the sensible and insensible wrenches in two case studies. The dimensions and the elasticity parameters of the simulated continuum robot are given in Table II. These values correspond to the robot in Fig. 1 and are used for the rest of this paper. d_{op} , d_{os} , d_{ip} , and d_{is} designate the outer and inner diameters for primary and secondary backbones, respectively.

Case study 1: $\boldsymbol{\psi} = [\theta_L = 90^\circ, \delta = 45^\circ]^T$.

An intuitive example can be reviewed when the robot is straight as in Fig. 6(A). This figure shows the pencil of sensible wrenches indicated by lines and the basis for the 4-D insensible wrenches shown by black arrows. The numerical values of $\mathbf{J}_{\mathbf{x}\psi}$, $\mathbf{U}_{\mathbf{x}}$, $\mathbf{D}_{\mathbf{x}}$, and $\mathbf{V}_{\mathbf{x}}$ are listed in Table III. Four conclusions are drawn about this case study.

- 1) One wrench (the third column in the corresponding $\mathbf{U}_{\mathbf{x}}$ matrix in Table III) is $[0 \ 0 \ 1 \ 0 \ 0 \ 0]^T$, which can be expressed as a screw with infinite pitch and does not appear in Fig. 6(A). It stands for a pure force in the Z -direction. It is insensible because the primary backbone is fixed to the base disk such that the load on it is not monitored by the load cells.
- 2) Another wrench (the sixth column in the corresponding $\mathbf{U}_{\mathbf{x}}$ matrix in Table III) is $[0 \ 0 \ 0 \ 0 \ 0 \ 1]^T$, which can be expressed as a screw with zero pitch and does not appear in Fig. 6(A) either. It stands for a pure moment in the Z -direction. It is insensible because at this configuration, the moment about $\hat{\mathbf{z}}_e$ does not affect the actuation.
- 3) The two arrows in Fig. 6(A) stand for the force–moment combinations, which will generate zero changes of the actuation forces on the joints level (the fourth and fifth columns in the corresponding $\mathbf{U}_{\mathbf{x}}$ matrix in Table III).
- 4) When the robot is straight, the force along $\hat{\mathbf{z}}_b$ and the moment about $\hat{\mathbf{z}}_b$ cannot be sensed. The sensible cylindroid appears as a flat pencil within the XY -plane, shown in Fig. 6(A), compared with the finite pitch cylindroid in Fig. 6(B). Matrix $\mathbf{D}_{\mathbf{x}}$ degrades to rank 1.

Case study 2: $\boldsymbol{\psi} = [\theta_L = 30^\circ, \delta = 45^\circ]^T$.

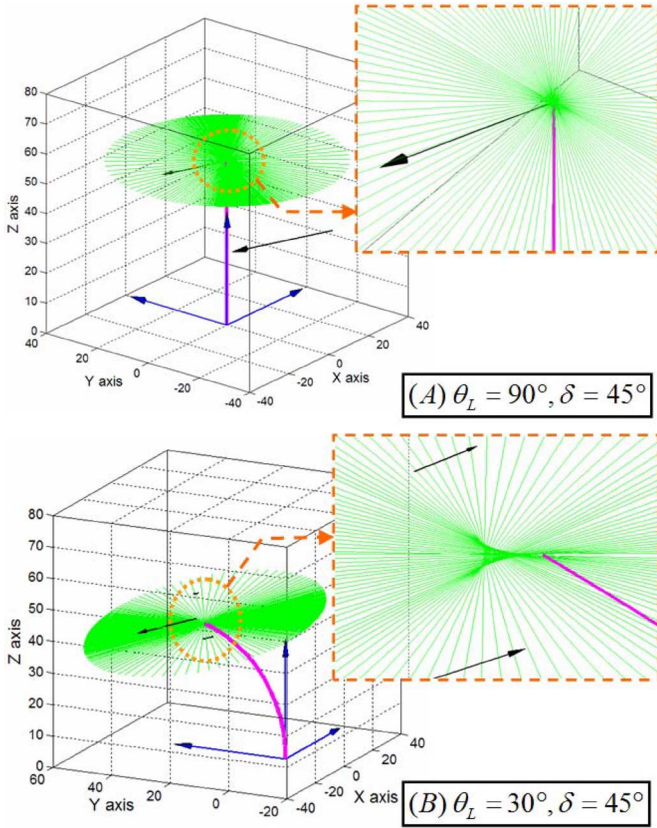


Fig. 6. Insensible wrenches (shown by arrows) and sensible wrench cylindroid (designated by lines) for two case studies.

TABLE III
NUMERICAL VALUES OF ENTITIES

	$\theta_L = 90^\circ, \delta = 45^\circ$	$\theta_L = 30^\circ, \delta = 45^\circ$
$\mathbf{J}_{x\psi}$	$\begin{bmatrix} -19.4454 & 0 \\ 19.4454 & 0 \\ 0 & 0 \\ -0.7071 & 0 \\ -0.7071 & 0 \\ 0 & 0 \end{bmatrix}$	$\begin{bmatrix} -14.4304 & -18.5690 \\ 14.4304 & -18.5690 \\ 17.1741 & 0 \\ -0.7071 & 0.6124 \\ -0.7071 & -0.6124 \\ 0 & -0.5000 \end{bmatrix}$
\mathbf{U}_x	$\begin{bmatrix} -.7066 & .7066 & 0 & -.0257 & -.0257 & 0 \\ .7066 & .7074 & 0 & .0106 & .0106 & 0 \\ 0 & 0 & 1.0000 & 0 & 0 & 0 \\ -.0257 & .0106 & 0 & .9996 & -.0004 & 0 \\ -.0257 & .0106 & 0 & -.0004 & .9996 & 0 \\ 0 & 0 & 0 & 0 & 0 & 1.0000 \end{bmatrix}$	$\begin{bmatrix} -.5406 & -.7066 & .4551 & -.0039 & -.0336 & -.0121 \\ .5406 & -.7066 & -.4548 & .0368 & .0006 & -.0148 \\ .6434 & .0000 & .7654 & .0070 & .0124 & .0022 \\ -.0265 & .0233 & .0132 & .9993 & -.0004 & .0001 \\ -.0265 & -.0233 & .0061 & .0001 & .9994 & -.0003 \\ 0 & -.0190 & -.0029 & .0003 & -.0001 & .9998 \end{bmatrix}$
\mathbf{V}_x	$\begin{bmatrix} 1 & 0 \\ 0 & 1 \end{bmatrix}$	$\begin{bmatrix} 1 & 0 \\ 0 & 1 \end{bmatrix}$
\mathbf{D}_x	$\begin{bmatrix} \text{diag}(27.5182, 0) \\ \mathbf{0}_{4 \times 2} \end{bmatrix}$	$\begin{bmatrix} \text{diag}(26.6912, 26.2796) \\ \mathbf{0}_{4 \times 2} \end{bmatrix}$

From the corresponding \mathbf{U}_x from Table III, four wrenches (the third to sixth columns in \mathbf{U}_x) are shown in Fig. 6(B). These four wrenches (black arrows) represent the basis for the insensible wrench space. The sixth column is very close to the wrench $[0 \ 0 \ 0 \ 0 \ 0 \ 1]^T$ so that it almost disappears in Fig. 6(B). This means that the continuum robot is indeed not good at esti-

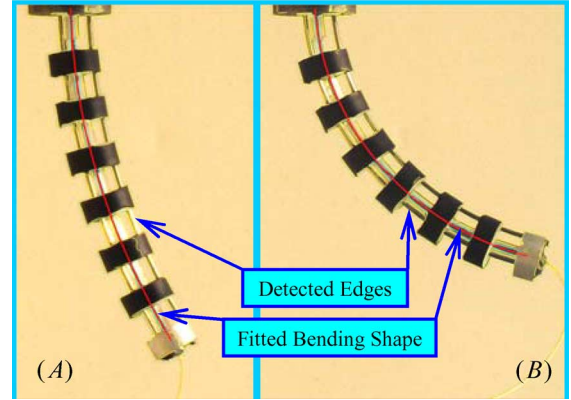


Fig. 7. Actual bending shape of the robot for configurations. (A) $\theta_L = 60^\circ$ and $\delta = 0^\circ$. (B) $\theta_L = 15^\circ$ $\delta = 0^\circ$.

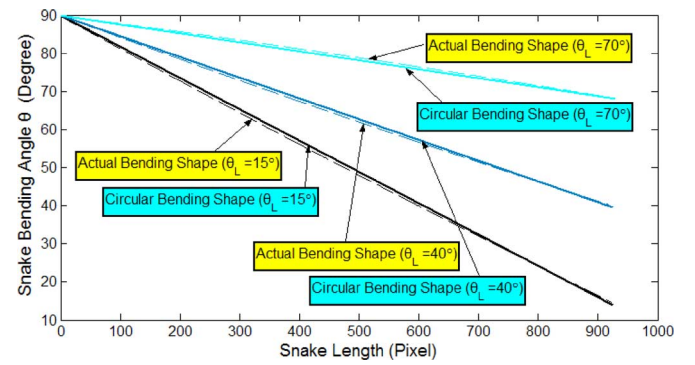


Fig. 8. Bending shape along the primary backbone of the continuum robot.

imating the moment about the $\hat{\mathbf{z}}_e$. This hereby forms a situation we should avoid in the path planning of the continuum robot.

The sensible wrenches (the first and second columns in the corresponding \mathbf{U}_x matrix in Table III) now form a 2-D cylindroid with a finite pitch [see Fig. 6(B)].

III. EXPERIMENTAL CORRECTIONS FOR THE MODELING

The model presented in the previous section assumes a perfectly circular bending shape of the robot. In this section, we validate this assumption and we propose necessary correction factors that account for shape discrepancy between the ideal model and the actual robot in Fig. 1. The necessary correction factor is subsequently applied to correct the kinematics and the force sensing models.

To gain some insight into the sources of the kinematics modeling errors, a series of pictures of the continuum robot shown in Fig. 1 were taken while the robot was bent to different angles. These pictures were transformed into gray scale, edges were detected using Canny masks [55], and then, a third-order polynomial was fitted to each bending shape of the continuum robot to parameterize the shape. The pictures of the robot bending to $\theta_L = 60^\circ, \delta = 0^\circ$ and $\theta_L = 15^\circ, \delta = 0^\circ$ are shown in Fig. 7(A) and (B), respectively.

Fig. 8 shows the actual shape of the primary backbone compared to a circular shape, when the actual end effector angle $\theta_L = 70^\circ, \theta_L = 40^\circ$, and $\theta_L = 15^\circ$. To quantitatively estimate how close the actual bending shape is to a circular arc, the actual

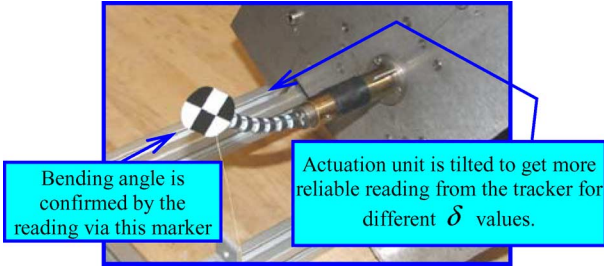


Fig. 9. Experimental setup used to confirm the end effector angle θ_L .

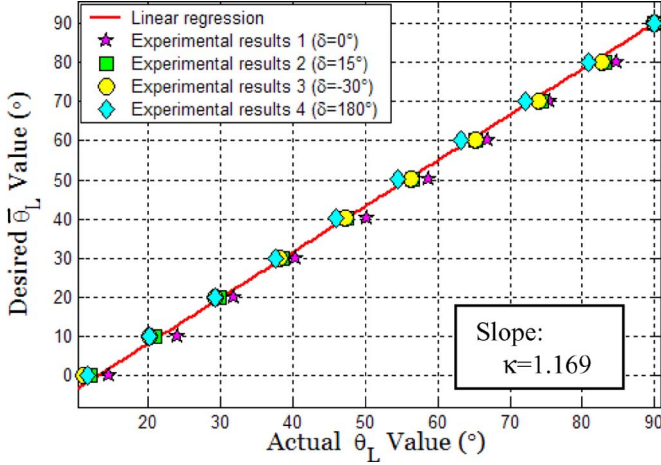


Fig. 10. Actual θ_L value versus desired $\bar{\theta}_L$ value.

tip position is calculated by an integral along the actual primary backbone shape. The results show that the robot tip position error is smaller than ± 0.5 mm. (The tip orientation error has been accounted since the θ_L in Fig. 8 is the actual value.)

A. No Correction Required on $\mathbf{J}_{x\psi}$

It has been previously shown in [2] that by assuming a characteristic bending shape of the continuum robot, a corresponding twist distribution can be used to parameterize the kinematics of the end effector in terms of its angle θ_L and δ . As a result, the Jacobian matrix $\mathbf{J}_{x\psi}$ depends on the bending shape of the continuum robot. We showed in Fig. 8 that these shape errors are within 0.5 mm while the length of the continuum robot is 50 mm (1% error). The constant radius-of-curvature approximation is acceptable and we will henceforth continue to use the nominal Jacobian matrix $\mathbf{J}_{x\psi}$ as given by (6) for our force sensing algorithm.

B. Corrections on $\mathbf{J}_{q\psi}$

When actuation commands were issued according to (1), the actual θ_L was larger than the desired value (less bending). A series of experiments were conducted using the experimental setup in Fig. 9. The actual θ_L was extracted from pictures as the ones shown in Fig. 7. The value was also confirmed from a marker reading using a Micron optical tracker (see Fig. 9). The actual versus the desired values of θ_L were plotted in Fig. 10. A linear regression was fitted to these experimental results and the result is given in (32), where $\bar{\theta}_L$ is the desired end effector

value, $\kappa = 1.169$, and $\theta_c = 15.21^\circ$:

$$\bar{\theta}_L = \kappa\theta_L - \theta_c. \quad (32)$$

The appearance of θ_c is due to defining the straight configuration as $\theta_L = \pi/2$. Based on the experimental results, (1) was corrected as

$$L_i = L + q_i = L + \Delta_i ((\kappa\theta_L - \theta_c) - \theta_0). \quad (33)$$

According to (33), the Jacobian matrix $\mathbf{J}_{q\psi}$ is corrected

$$\mathbf{J}_{q\psi} = \begin{bmatrix} \kappa r \cos(\delta), & -r(\kappa\theta_L - \theta_c - \theta_0) \sin(\delta) \\ \kappa r \cos\left(\delta + \frac{2\pi}{3}\right), & -r(\kappa\theta_L - \theta_c - \theta_0) \sin\left(\delta + \frac{2\pi}{3}\right) \\ \kappa r \cos\left(\delta + \frac{4\pi}{3}\right), & -r(\kappa\theta_L - \theta_c - \theta_0) \sin\left(\delta + \frac{4\pi}{3}\right) \end{bmatrix}. \quad (34)$$

The source of this actuation error could be the machining tolerances of the holes in the spacer disks and the base disk, local deformation of the backbones in segments lying between the spacer disks, etc.

C. Applying the Correction to the Statics Model

The correction in (33) will also lead to corrections in the statics model of the continuum robot. Equation (10) needs to be updated using (33), so does (13). The gradient of the elastic energy $\nabla \mathbf{E}$ is updated as the following, using L_i from (33)

$$\begin{aligned} \nabla \mathbf{E} &= \begin{bmatrix} (\theta_L - \theta_0) \left(\frac{E_p I_p}{L} + \sum_{i=1}^3 \frac{E_s I_s}{L_i} \right) - \frac{(\theta_L - \theta_0)^2}{2} E_s I_s r \sum_{i=1}^3 \frac{\kappa \cos \delta_i}{L_i^2} \\ \frac{(\theta_L - \theta_0)^3}{2} E_s I_s r \sum_{i=1}^3 \frac{\sin \delta_i (\kappa\theta_L - \theta_c - \theta_0)}{L_i^2} \end{bmatrix}. \end{aligned} \quad (35)$$

IV. EXPERIMENTAL VALIDATION

To validate the proposed force sensing model, we setup two experiments. In the first experiment, calibration weights were used to apply forces at the end disk. In the second experiment, the robot was used to detect the stiffness of a flexible silicone strip that serves as a mockup tissue.

A. Experiment 1: Sensing Forces Applied at the End Disk

Fig. 11 shows the experimental setup. A Kevlar thread was attached to the tip of the robot so that a pure force can be applied. The force was applied through a frictionless pulley, using calibrated weights. The pulley was mounted to an aluminum frame, which was set such that the applied force is always parallel to the XY -plane of BDS. A marker was aligned with the Kevlar thread to measure the direction of the applied force using an optical tracker. The marker is printed on paper and it weighs 0.12 g. Adding this marker would not disturb the experimental results. The actuation unit of the robot was repositioned when

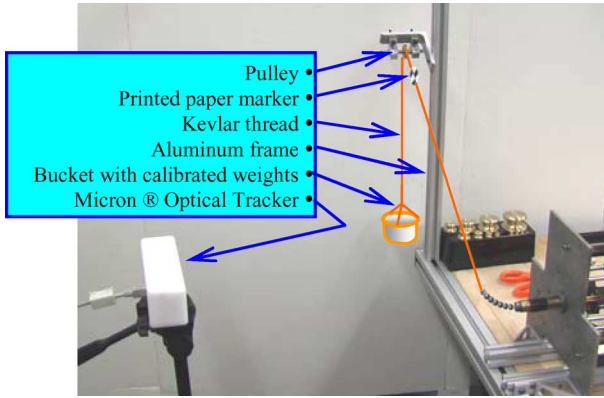


Fig. 11. Experimental setup used for validation of the force sensing model.

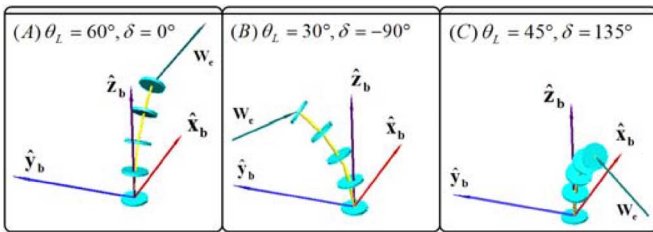


Fig. 12. Robot configurations used in the force sensing experiments.

the robot was bent to different θ_L values in order to keep the force parallel to the XY -plane of the BDS.

The robot was bent to different configurations. Under each configuration, known forces $[W_e$ in Fig. 12(A)–(C)] were applied at the center of the end disk. The applied force varies from 5.4 to 55.4 g in the increment of 10 g. The actuation forces on the secondary backbones were monitored using Omega LC703 load cells coupled with a 12-bit A/D at ± 0.01 V measurement range. This experimental setup allowed an actuation force measurement with a resolution of ± 0.5 g. However, since there is some small friction in the reading, the actual resolution is estimated to be about ± 10 g.

Since the applied force on the end disk was always parallel to the XY -plane of the BDS, this external information was used in (17) to obtain the best estimate of W_e . We solved (19) with $S_e = \text{diag}(0, 0, 1, 1, 1, 1)$ and $W_{se} = [1 \ 1 \ 0 \ 0 \ 0 \ 0]^T$. The experiments were repeated three times for each robot configuration to validate repeatability. The results are listed in Table IV and plotted in Fig. 13. The table lists the averages of the three experimental results and the corresponding errors. Among the error values, the average was 0.34 g with a standard deviation of 0.83 g. Fig. 13 plots all the actual forces and the experimental results in the XY -plane of BDS.

To be noted, with a resolution of ± 10 g at the joint level force monitoring, a precision of 0.34 ± 0.83 g was obtained. This was due to the superiority of this novel design. Substituting (24) into (17), the magnitude of τ as well as its reading uncertainty $\Delta\tau$ was reduced by a factor from \tilde{D}_x , since U_x and V_x^T are both orthogonal matrices. Referring to the diagonal values of D_x in Table II, the factor is about 27, which means an error of $0.34 \pm$

TABLE IV
EXPERIMENTAL RESULTS (IN GRAMS)

$\theta_L = 60^\circ, \delta = 0^\circ$ (X and Y component in grey and white cells, respectively)					
Actual Force		Sensed Force Average		Error	
5.39	-0.36	6.74	0.36	-1.35	-0.73
15.37	-1.02	16.85	-0.55	-1.49	-0.47
25.34	-1.68	25.58	-1.86	-0.24	0.18
35.32	-2.35	34.32	-3.10	1.01	0.75
45.30	-3.01	43.59	-4.31	1.71	1.30
55.28	-3.67	52.80	-5.45	2.48	1.78
$\theta_L = 30^\circ, \delta = -90^\circ$ (X and Y component in grey and white cells, respectively)					
Actual Force		Sensed Force Average		Error	
4.62	-2.80	4.40	-2.29	0.22	-0.50
13.17	-7.98	12.05	-7.36	1.12	-0.62
21.73	-13.16	21.40	-13.68	0.32	0.52
30.28	-18.34	29.87	-18.99	0.41	0.65
38.83	-23.52	38.96	-24.35	-0.12	0.84
47.39	-28.70	47.70	-29.94	-0.32	1.24
$\theta_L = 45^\circ, \delta = 135^\circ$ (X and Y component in grey and white cells, respectively)					
Actual Force		Sensed Force Average		Error	
4.10	3.51	3.74	3.21	0.36	0.30
11.69	10.02	11.38	9.44	0.31	0.58
19.29	16.53	19.37	16.52	-0.09	0.01
26.88	23.04	26.75	22.82	0.13	0.21
34.47	29.55	34.02	29.64	0.45	-0.10
42.06	36.05	40.88	35.91	1.18	0.15

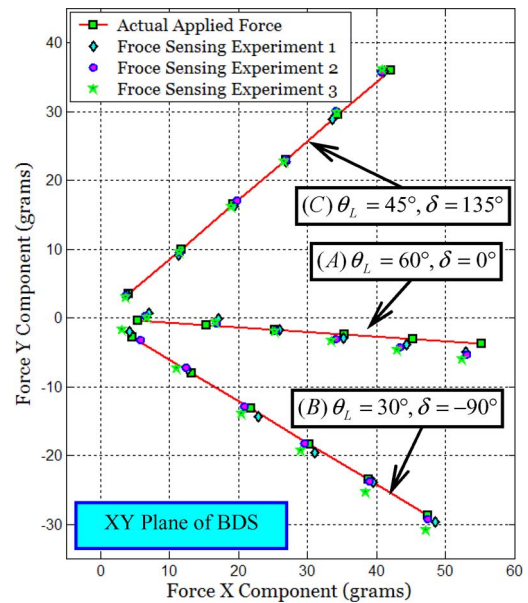


Fig. 13. Experimental results for force measurements corresponding to the configurations shown in Fig. 12.

0.83 g is equivalent to about 9.18 ± 22.41 g at the joint-level reading errors.

B. Experiment II: Stiffness Detection for a Mockup Tissue

A silicone strip was molded with three steel balls embedded in it [see Fig. 14(A)]. The ball diameters were 6.34, 9.51, and 12.69 mm, respectively. They were embedded at a depth of 0.5 mm from the probed surface, as shown in Fig. 14(B). The silicone strip was probed using our robot (see Fig. 14). The probing depth was 0.5 mm. A Cartesian XYZ stage was used to

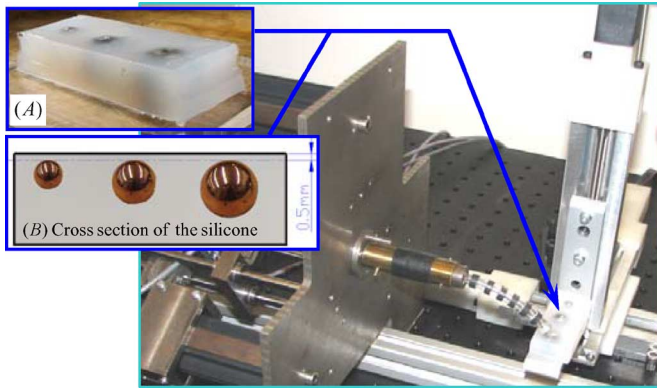


Fig. 14. Experimental setup for stiffness detection of a mockup tissue. (A) Silicone rubber strip with three steel balls in it. (B) Cross-sectional view.

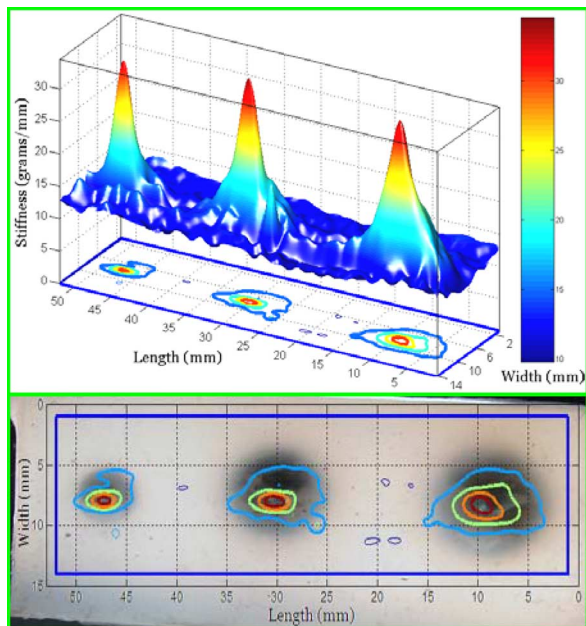


Fig. 15. Detected stiffness map of the silicone strip in Fig. 14.

adjust the position of the silicone strip so that the workspace of the continuum robot can cover the entire surface of this silicone strip. The surface was scanned with 1 mm increment both in length and in width directions. The stiffness value on a probed point was calculated as the ratio of resistance force over probed depth of 0.5 mm. The resistance force is calculated with $\mathbf{S}_e = \text{diag}(0, 0, 1, 1, 1, 1)$ and $\mathbf{W}_{se} = [1 \ 1 \ 0 \ 0 \ 0 \ 0]^T$, since the resistance force is normal to the surface of the silicone strip, which is parallel to \hat{x}_b , as shown in Fig. 14. The entire surface stiffness map was then generated using spline interpolation (see Fig. 15). In Fig. 15, the contour of the surface stiffness map is overlaid beneath the stiffness surface as well as on top of the real silicone strip.

From Fig. 15, the three stiffness peaks correspond to the three embedded balls. Different slopes of the peaks and different sizes of the stiffness contours tell that the three balls are different in size. The same height of the three stiffness peaks for all three balls means that the balls are embedded at the approximate same

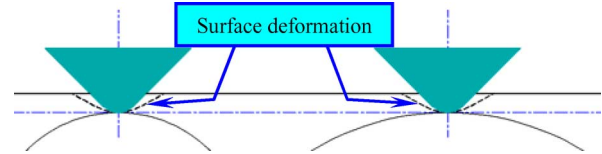


Fig. 16. Stiffness probing of the silicone strip in Fig. 14.

depth. The reason is explained in Fig. 16. The silicone was not probed deep enough to induce large motion of the balls inside the silicone. The resistance force sensed by robot comes from the local surface deformation of the silicone strip. This superior force sensing sensitivity gives the robot the ability to detect not only the shape but also the depth of embedded objects.

Since the low-cost silicone is manually mixed and naturally cured, the stiffness over the surface is not uniform. It explains why there are some little spikes in the stiffness map in Fig. 15.

V. CONCLUSION

Force sensing can help surgical tools to improve patient safety and operation precision in MIS dealing with soft organs. However, medical or size requirements sometimes prevent the implementation of traditional multi-axis force sensors at the tip of the surgical instruments. An alternative approach was explored in this paper. This approach used the intrinsic force sensing ability of flexible continuum robots based on joint-level force information.

The theoretical study of the force sensing capabilities of a continuum robot was based on the SVD of a Jacobian matrix that maps speeds from a 2-D configuration space to twists in 6-D space. Using the SVD we proved that the wrenches that cannot be sensed belong to a 4-D wrench system while the sensible wrenches belong to a 2-D cylindroid. We also presented a force sensing solution that accounts for external information coming from knowledge about some components of the external wrench or from external sensors.

Using screw theory, we presented two simulation case studies with the corresponding visualization of the sensible wrenches. The theoretical analysis was validated through experiments. The force sensing errors have been shown to have an average of 0.34 g with a standard deviation of 0.83 g. Stiffness maps of an unknown mockup tissue were generated and hard objects were effectively detected.

We believe that this suggests the strong potential for using these continuum robots for surgical applications that require force feedback in confined spaces, such as the highly dexterous flexible snake-like device for MIS of the throat and the upper airways [2], [23], [25], [26], [56]. This theoretical model is currently being extended to multisection snake-like devices, where the coupling effects of adjacent sections remain to be investigated.

APPENDIX A

The position and orientation of the end disk relative to the base disk is characterized by two angles θ_L and δ . The angles

δ_i ($i = 1, 2,$ and 3) are related to δ according to (36)

$$\delta_i = \delta + (i - 1)\beta. \quad (36)$$

The projection of the i^{th} secondary backbone on the bending plane is a curve offset by $\Delta_i \in [-r, r]$ from the primary backbone. The radius of curvature and arc-length of this curve are, respectively, indicated by $\rho_i(s_i)$ and s_i , and are related to the parameters of the primary backbone according to

$$\rho(s) = \rho_i(s) + \Delta_i \quad (37)$$

where $\Delta_i \equiv r \cos(\delta_i)$.

The length of the primary backbone and the length of the i^{th} backbone are related according to

$$L_i = \int ds_i = \int ds_i - ds + ds = L + \int_{\theta_0}^{\theta_L} (\rho_i(s) - \rho(s))d\theta. \quad (38)$$

Using (38) yields (1).

APPENDIX B

Since $\mathbf{J}_{x\psi}$ is formulated as

$$\begin{bmatrix} \mathbf{J}_{p\psi} \\ \mathbf{J}_{\omega\psi} \end{bmatrix}$$

$\mathbf{J}_{p\psi}$ can be found by taking time derivative of ${}^b\mathbf{p}$, as in (41), while $\mathbf{J}_{\omega\psi}$ is found by formulating the angular velocity of GCS [see (43)]. ${}^1\mathbf{p}$ is the position of the tip of the continuum robot in the BPS, which can be derived according to the geometry shown in Fig. 2:

$${}^b\mathbf{p} = {}^b\mathbf{R}_1 {}^1\mathbf{p} \quad (39)$$

$${}^1\mathbf{p} = \frac{L \begin{bmatrix} \sin \theta_L - \sin \theta_0 & 0 & \cos \theta_0 - \cos \theta_L \end{bmatrix}^T}{-(\theta_0 - \theta_L)} \quad (40)$$

$$\mathbf{J}_{p\psi} = L \begin{bmatrix} c_\delta \frac{(\theta_L - \theta_0)c_{\theta_L} - s_{\theta_L} + 1}{(\theta_L - \theta_0)^2} & -\frac{s_\delta(s_{\theta_L} - 1)}{\theta_L - \theta_0} \\ -s_\delta \frac{(\theta_L - \theta_0)c_{\theta_L} - s_{\theta_L} + 1}{(\theta_L - \theta_0)^2} & -\frac{c_\delta(s_{\theta_L} - 1)}{\theta_L - \theta_0} \\ \frac{(\theta_L - \theta_0)s_{\theta_L} + c_{\theta_L}}{(\theta_L - \theta_0)^2} & 0 \end{bmatrix} \quad (41)$$

$${}^b\boldsymbol{\omega}_g = -\dot{\delta}\hat{\mathbf{z}}_b + {}^b\mathbf{R}_1(-\dot{\theta}_L {}^1\hat{\mathbf{y}}_1 + {}^1\mathbf{R}_e(\dot{\delta}^e\hat{\mathbf{z}}_e)) \quad (42)$$

$$\mathbf{J}_{\omega\psi} = \begin{bmatrix} -s_\delta & c_\delta c_{\theta_L} \\ -c_\delta & -s_\delta c_{\theta_L} \\ 0 & -1 + s_{\theta_L} \end{bmatrix}. \quad (43)$$

REFERENCES

- [1] R. H. Taylor, J. Funda, B. Eldridge, S. Gomory, K. Gruben, D. LaRose, M. Talamini, L. Kavoussi, and J. Anderson, "A telerobotics assistant for laparoscopic surgery," *IEEE Eng. Med. Biol. Mag.*, vol. 14, no. 3, pp. 279–288, May/June 1995.
- [2] N. Simaan, R. H. Taylor, and P. Flint, "A dexterous system for laryngeal surgery—Multi-backbone bending snake-like slaves for teleoperated dexterous surgical tool manipulation," in *Proc. IEEE Int. Conf. Robot. Autom. (ICRA)*, New Orleans, LA, 2004, pp. 351–357.
- [3] S. T. Charles, H. Das, T. Ohm, C. Boswell, G. Rodriguez, and R. Steele, "Dexterity-enhanced telerobotic microsurgery," in *Proc. IEEE Int. Conf. Adv. Robot. (ICAR)*, Monterey, CA, 1997, pp. 5–10.
- [4] M. Minor and R. Mukherejee, "A dexterous manipulator for minimally invasive surgery," in *Proc. IEEE Int. Conf. Robot. Autom. (ICRA)*, Detroit, MI, 1999, pp. 2057–2064.
- [5] H. Yamashita, D. Kim, N. Hata, and T. Dohi, "Multi-slider linkage mechanism for endoscopic forceps manipulator," in *Proc. IEEE/RSJ Int. Conf. Intell. Robots Syst. (IROS)*, Las Vegas, NV, 2003, pp. 2577–2582.
- [6] A. Yagi, K. Matsumiya, K. Masamune, H. Liao, and T. Dohi, "Rigid-flexible outer sheath model using slider linkage locking mechanism and air pressure for endoscopic surgery," in *Proc. Int. Conf. Med. Image Comput. Comput.-Assisted Intervention (MICCAI)*, Copenhagen, Denmark, 2006, pp. 503–510.
- [7] S. Ma, I. Kobayashi, S. Hirose, and K. Yokoshima, "Control of a multijoint manipulator 'Moray Arm'," *IEEE/ASME Trans. Mechatron.*, vol. 7, no. 3, pp. 304–317, Sep. 2002.
- [8] J.-P. Merlet, "Optimal design for the micro parallel robot MIPS," in *Proc. IEEE Int. Conf. Robot. Autom. (ICRA)*, Washington, DC, 2002, pp. 1149–1154.
- [9] C. Reboulet and S. Durand-Leguay, "Optimal design of redundant parallel mechanism for endoscopic surgery," in *Proc. IEEE/RSJ Int. Conf. Intell. Robots Syst. (IROS)*, Kyongju, South Korea, 1999, pp. 1432–1437.
- [10] D. Asai, S. Katopo, J. Arata, S. I. Warisawa, M. Mitsuishi, A. Morita, S. Sora, T. Kirino, and R. Mochizuki, "Micro-neurosurgical system in the deep surgical field," in *Proc. Int. Conf. Med. Image Comput. Comput.-Assisted Intervention (MICCAI)*, Saint-Malo, France, 2004, pp. 33–40.
- [11] A. J. Madhani, G. Niemeyer, and K. J. Salisbury, "The black falcon: A teleoperated surgical instrument for minimally invasive surgery," in *Proc. IEEE/RSJ Int. Conf. Intell. Robots Syst. (IROS)*, Victoria, Canada, BC, 1998, pp. 936–944.
- [12] P. S. Schenker, E. C. Barlow, C. D. Boswell, H. Das, S. Lee, T. Ohm, E. Paljug, G. Rodriguez, and S. T. Charles, "Development of a telemanipulator for dexterity enhanced microsurgery," in *Proc. 2nd Annu. Int. Symp. Med. Robot. Comput. Assisted Surg. (MRCAS)*, Baltimore, MD, 1995, pp. 81–88.
- [13] P. Dario, M. C. Carrozza, and A. Pietrabissa, "Development and in vitro testing of a miniature robotic system for computer-assisted colonoscopy," *Comput. Aided Surg.*, vol. 4, pp. 1–14, 1999.
- [14] P. Dario, C. Paggetti, N. Troisfontaine, E. Papa, T. Ciucci, M. C. Carrozza, and M. Marcacci, "A miniature steerable end-effector for application in an integrated system for computer-assisted arthroscopy," in *Proc. IEEE Int. Conf. Robot. Autom. (ICRA)*, Albuquerque, NM, 1997, pp. 1573–1579.
- [15] K. Harada, K. Tsubouchi, M. G. Fujie, and T. Chiba, "Micro manipulators for intrauterine fetal surgery in an open MRI," in *Proc. IEEE Int. Conf. Robot. Autom. (ICRA)*, Barcelona, Spain, 2005, pp. 504–509.
- [16] K. Ikuta, K. Yamamoto, and K. Sasaki, "Development of remote microsurgery robot and new surgical procedure for deep and narrow space," in *Proc. IEEE Int. Conf. Robot. Autom. (ICRA)*, Taipei, Taiwan, 2003, pp. 1103–1108.
- [17] J. Peirs, D. Reynaerts, and H. Van Brussel, "Design of miniature parallel manipulators for integration in a self-propelling endoscope," *Sens. Actuators A, Phys.*, vol. 85, pp. 409–417, 2000.
- [18] D. Reynaerts, J. Peirs, and H. Van Brussel, "Shape memory micro-actuation for a gastro-intestinal intervention system," *Sens. Actuators A, Phys.*, vol. 77, pp. 157–166, 1999.
- [19] A. Degani, H. Choset, A. Wolf, T. Ota, and M. A. Zenati, "Percutaneous intrapericardial interventions using a highly articulated robotic probe," in *Proc. IEEE/RAS-EMBS Int. Conf. Biomed. Robot. Biomechatron.*, Pisa, Italy, 2006, pp. 7–12.
- [20] A. Degani, H. Choset, A. Wolf, and M. A. Zenati, "Highly articulated robotic probe for minimally invasive surgery," in *Proc. IEEE Int. Conf. Robot. Autom. (ICRA)*, Orlando, FL, 2006, pp. 4167–4172.
- [21] H. Yamashita, N. Hata, M. Hashizume, and T. Dohi, "Handheld laparoscopic forceps manipulator using multi-slider linkage mechanisms," in *Proc. Int. Conf. Med. Image Comput. Comput.-Assisted Intervention (MICCAI)*, St. Malo, France, 2004, pp. 121–128.
- [22] G. S. Guthart and K. J. Salisbury, "The Intuitive telesurgery system: Overview and application," in *Proc. IEEE Int. Conf. Robot. Autom. (ICRA)*, San Francisco, CA, 2000, pp. 618–621.
- [23] A. Kapoor, N. Simaan, and R. H. Taylor, "Suturing in confined spaces: Constrained motion control of a hybrid 8-DoF robot," in *Proc. Int. Conf. Adv. Robot. (IACR)*, Seattle, WA, 2005, pp. 452–459.

- [24] N. Simaan, R. Taylor, and P. Flint, "High dexterity snake-like robotic slaves for minimally invasive telesurgery of the upper airway," in *Proc. Int. Conf. Med. Image Comput. Comput.-Assisted Intervention (MICCAI)*, St. Malo, France, 2004, pp. 17–24.
- [25] N. Simaan, "Snake-like units using flexible backbones and actuation redundancy for enhanced miniaturization," in *Proc. IEEE Int. Conf. Robot. Autom. (ICRA)*, Barcelona, Spain, 2005, pp. 3012–3017.
- [26] K. Xu and N. Simaan, "Actuation compensation for flexible surgical snake-like robots with redundant remote actuation," in *Proc. IEEE Int. Conf. Robot. Autom. (ICRA)*, Orlando, FL, 2006, pp. 4148–4154.
- [27] L. N. Verner and A. M. Okamura, "Sensor/actuator asymmetries in telemanipulators: Implications of partial force feedback," in *Proc. Symp. Haptic Interfaces Virtual Environ. Teleoperator Syst. (HAPTICS 2006)*, Alexandria, VA, pp. 309–314.
- [28] M. C. Cavusoglu, A. Sherman, and F. Tendick, "Design of bilateral teleoperation controllers for haptic exploration and telemanipulation of soft environments," *IEEE Trans. Robot. Autom.*, vol. 18, no. 4, pp. 641–647, Aug. 2002.
- [29] F. Tendick, M. C. Cavusoglu, N. Dhruv, and A. Sherman, "Maximizing the sensation of compliance in teleoperative surgery," presented at the Int. Symp. Robot. Appl. (ISORA), Maui, HI, 2000.
- [30] C. Wagner, N. Stylopoulos, and R. Howe, "The role of force feedback in surgery: Analysis of blunt dissection," in *Proc. 10th Symp. Haptic Interfaces Virtual Environ. Teleoperator Syst.*, 2002, pp. 68–74.
- [31] M. Mahvash and A. M. Okamura, "Friction compensation for a force-feedback telerobotic system," in *Proc. IEEE Int. Conf. Robot. Autom. (ICRA)*, Orlando, FL, 2006, pp. 3268–3273.
- [32] A. M. Okamura, "Methods for haptic feedback in teleoperated robot-assisted surgery," *Int. J. Ind. Robot*, vol. 31, pp. 499–508, 2006.
- [33] K. Ikuta, S. Daifu, T. Hasegawa, and H. Higashikawa, "Hyper-finger for remote minimally invasive surgery in deep area," in *Proc. Int. Conf. Med. Image Comput. Comput.-Assisted Intervention (MICCAI)*, Tokyo, Japan, 2002, pp. 173–181.
- [34] M. Tavakoli, R. V. Patel, and M. Moallem, "A force reflective master-slave system for minimally invasive surgery," in *Proc. Int. Conf. Intell. Robots Syst.*, Las Vegas, NV, 2003, pp. 3077–3082.
- [35] S. Shimachi, Y. Fujiwara, and Y. Hakozaki, "New sensing method of force acting on instrument for laparoscopic robot surgery," in *Comput. Assisted Radiol. Surg.*, Chicago, IL, 2004, pp. 775–780.
- [36] U. Seibold, B. Kubler, and G. Hirzinger, "Prototype of instrument for minimally invasive surgery with 6-axis force sensing capability," in *Proc. IEEE Int. Conf. Robot. Autom. (ICRA)*, Barcelona, Spain, 2005, pp. 496–501.
- [37] K. Tadano and K. Kawashima, "Development of 4-DoFs forceps with force sensing using pneumatic servo system," in *Proc. IEEE Int. Conf. Robot. Autom. (ICRA)*, Orlando, FL, 2006, pp. 2250–2255.
- [38] M. Mitsuishi, N. Sugita, and P. Pitakwatchara, "Force feedback augmentation modes in the laparoscopic minimal invasive telesurgical system," *IEEE/ASME Trans. Mechatron.*, vol. 12, no. 4, pp. 447–454, Aug. 2007.
- [39] S. Hirose, *Biologically Inspired Robots, Snake-Like Locomotors and Manipulators*. London, U.K.: Oxford Univ. Press, 1993.
- [40] I. A. Gravagne and I. D. Walker, "Kinematic transformations for remotely-actuated planar continuum robots," in *Proc. IEEE Int. Conf. Robot. Autom. (ICRA)*, 2000, pp. 19–26.
- [41] I. A. Gravagne and I. D. Walker, "Manipulability, force and compliance analysis for planar continuum manipulators," *IEEE Trans. Robot. Autom.*, vol. 18, no. 3, pp. 263–273, Jun. 2002.
- [42] G. S. Chirikjian and J. W. Burdick, "Kinematically optimal hyper-redundant manipulator configurations," *IEEE Trans. Robot. Autom.*, vol. 11, no. 6, pp. 794–806, Dec. 1995.
- [43] K. Zanganeh and J. Angeles, "The inverse kinematics of hyper-redundant manipulators using splines," in *Proc. IEEE Int. Conf. Robot. Autom. (ICRA)*, Nagoya, Japan, 1995, pp. 2797–2802.
- [44] G. S. Chirikjian, "Hyper-redundant manipulator dynamics: A continuum approximation," *Adv. Robot.*, vol. 9, pp. 217–243, 1995.
- [45] H. Mochiyama, E. Shimemura, and H. Kobayashi, "Shape control of manipulators with hyper degrees of freedom," *Int. J. Robot. Res.*, vol. 18, pp. 584–600, 1999.
- [46] I. A. Gravagne and I. D. Walker, "On the kinematics of remotely-actuated continuum robots," in *Proc. IEEE Int. Conf. Robot. Autom. (ICRA)*, San Francisco, CA, 2000, pp. 2544–2550.
- [47] B. A. Jones and I. D. Walker, "Practical kinematics for real-time implementation of continuum robots," *IEEE Trans. Robot. Autom.*, vol. 22, no. 6, pp. 1087–1099, Dec. 2006.
- [48] R. P. Paul, *Robot Manipulators: Mathematics, Programming, and Control*. Cambridge, MA: MIT Press, 1981.
- [49] D. G. Fertis, *Advanced Mechanics of Structure*. New York: Marcel Dekker, 1996.
- [50] M. T. Mason and K. J. Salisbury, *Robot Hands and the Mechanics of Manipulation*. Cambridge, MA: MIT Press, 1985.
- [51] V. C. Klema and A. J. Laub, "The singular value decomposition: Its computation and some applications," *IEEE Trans. Autom. Control*, vol. AC-25, no. 2, pp. 164–176, Apr. 1980.
- [52] L.-W. Tsai, *Robot Analysis: The Mechanics of Serial and Parallel Manipulators*. New York: Wiley, 1999.
- [53] H. Pottmann and J. Wallner, *Computational Line Geometry*. New York: Springer-Verlag, 2001.
- [54] K. H. Hunt, *Kinematic Geometry of Mechanisms*. Oxford, U.K.: Clarendon, 1978.
- [55] B. Horn, *Robot Vision*. Cambridge, MA: MIT Press, 1986.
- [56] A. Kapoor, N. Simaan, and P. Kazanzides, "A system for speed and torque control of DC motors with application to small snake robots," presented at the IEEE Conf. Mechatron. Robot. (MECHROB). Aachen, Germany, 2004.



Kai Xu (S'05) received the B.E. and M.S. degrees in machine design, manufacture and automation from Tsinghua University, Beijing, China, in 2001 and 2004, respectively. He is currently working toward the Ph.D. degree in the Department of Mechanical Engineering, Columbia University, New York.

His current research interests include continuum robots, medical robotics, smart surgical tool synthesis, and control systems.

Mr. Xu is the recipient of the Distinguished Presidential Fellowship from the Fu Foundation School of Engineering and Applied Sciences, Columbia University.



Nabil Simaan (M'04) received the B.Sc., M.Sc., and Ph.D. degrees in mechanical engineering from the Technion—Israel Institute of Technology, Haifa, Israel, in 1996, 1999, and 2002, respectively.

During 2003, he was a Postdoctoral Research Scientist at Johns Hopkins University National Science Foundation (NSF) Engineering Research Center for Computer-Integrated Surgical Systems and Technology (ERC-CISST), where he was engaged in research on minimally invasive robotic assistance in confined spaces. Since 2005, he has been an Assistant Professor in the Department of Mechanical Engineering, Columbia University, New York, where he has also been the Director of the Advanced Robotics and Mechanisms Applications (ARMA) Laboratory, and was engaged in designing and constructing compact parallel robots for medical applications and compact and down-scalable surgical slaves for minimally invasive surgery of the throat and upper airway. His current research interests include synthesis of novel robotic systems for surgical assistance in confined spaces with applications to minimally invasive surgery of the throat, natural orifice surgery, cochlear implant surgery, and dexterous bimanual microsurgery.